Article:

eprints@whiterose.ac.uk
https://eprints.whiterose.ac.uk/

Measurement of the cosmogenic activation of germanium detectors in EDELWEISS-III

E. Armengaud[a], Q. Arnaud[b,1], C. Augier[b], A. Benoît[c], L. Bergé[d],
J. Billard[b], J. Blümer[e,f], T. de Boissière[a], A. Broniatowski[d,e], P. Camus[c],
A. Cazes[b], M. Chapellier[d], F. Charlieux[b], M. De Jésus[b], L. Dumoulin[d],
K. Eitel[f], N. Foerster[e], J. Gascon[b], A. Giuliani[d], M. Gros[a], L. Hehn[f],
G. Heuermann[e], Y. Jin[g], A. Juillard[b], C. Kéfélian[b,e], M. Kleifges[h],
V. Kozlov[f], H. Kraus[i], V. A. Kudryavtsev[j], H. Le-Sueur[d], S. Marnieros[d],
X.-F. Navick[a], C. Nones[a], E. Olivieri[d], P. Pari[k], B. Paul[a], M.-C. Piro[d,2],
D. Poda[d], E. Queguiner[b], S. Rozov[l], V. Sanglard[b], B. Schmidt[f,3],
S. Scorza[e,*], B. Siebenborn[f], D. Tcherniakhovski[h], L. Vagneron[b],
M. Weber[h], E. Yakushev[l]

[a]CEA Saclay, DSM/IRFU, 91191 Gif-sur-Yvette Cedex, France
[b]Univ Lyon, Université Claude Bernard Lyon 1, CNRS-IN2P3, Institut de Physique
Nucléaire de Lyon, F-69622, Villeurbanne, France
[c]Institut Néel, CNRS/UJF, 25 rue des Martyrs, BP 166, 38042 Grenoble, France
[d]CSNSM, Univ. Paris-Sud, CNRS/IN2P3, Université Paris-Saclay, 91405 Orsay, France
[e]Karlsruher Institut für Technologie, Institut für Experimentelle Kernphysik, Gaedestr.
1, 76128 Karlsruhe, Germany
[f]Karlsruher Institut für Technologie, Institut für Kernphysik, Postfach 3640, 76021
Karlsruhe, Germany
[g]Laboratoire de Photonique et de Nanostructures, CNRS, Route de Nozay, 91460
Marcoussis, France
[h]Karlsruher Institut für Technologie, Institut für Prozessdatenverarbeitung und
Elektronik, Postfach 3640, 76021 Karlsruhe, Germany
[i]University of Oxford, Department of Physics, Keble Road, Oxford OX1 3RH, UK
[j]University of Sheffield, Department of Physics and Astronomy, Sheffield, S3 7RH, UK
[k]CEA Saclay, DSM/IRAMIS, 91191 Gif-sur-Yvette Cedex, France
[l]JINR, Laboratory of Nuclear Problems, Joliot-Curie 6, 141980 Dubna, Moscow Region,
Russian Federation

*Corresponding author: silvia.scorza@kit.edu
[1]Now at Queen's University, Kingston, Canada
[2]Now at Rensselaer Polytechnic Institute, Troy, NY, USA
[3]Now at Lawrence Berkeley National Laboratory, Berkeley, CA, USA

Abstract

We present a measurement of the cosmogenic activation in the germanium cryogenic detectors of the EDELWEISS III direct dark matter search experiment. The decay rates measured in detectors with different exposures to cosmic rays above ground are converted into production rates of different isotopes. The measured production rates in units of nuclei/kg/day are 82 ± 21 for ^{3}H, 2.8 ± 0.6 for ^{49}V, 4.6 ± 0.7 for ^{55}Fe, and 106 ± 13 for ^{65}Zn. These results are the most accurate for these isotopes. A lower limit on the production rate of ^{68}Ge of 74 nuclei/kg/day is also presented. They are compared to model predictions present in literature and to estimates calculated with the ACTIVIA code.

Keywords: Germanium detector, Cosmogenic activation, Dark matter detection

1. Introduction

Germanium is widely used as a detector material in experiments searching for a rare process like the interaction of weakly interacting massive particles (WIMPs) [1]. It is possible to build detectors with very good energy resolution based on the measurement of the ionization produced in the particle interaction, or of the increase of temperature [2]. In addition, the combination of the ionization and heat signals is a powerful tool to distinguish nuclear recoils from electron recoils. Moreover, the crystal-growing process used in the semiconductor industry purifies the material to a high level that matches well the stringent ultra-low radioactivity requirements of rare event searches.

The potential of germanium detectors for achieving very low threshold below 1 keV is particularly attractive for searches of WIMPs with masses below $10\,\mathrm{GeV/c^2}$. The background at energies below 20 keV in such a detector is thus of particular interest. Notably, the contribution from tritium beta decays may have a significant impact on the sensitivity of the next generation of these detectors.

The crystallization process removes all cosmogenically-produced radioactive atoms, with the exception of unstable germanium isotopes like ^{68}Ge (see below). Their populations grow back again when the crystal is kept above ground, and therefore exposed to cosmic rays and the associated hadronic showers. Short-lived isotopes decay rapidly as soon as the detectors are

stored underground, deep enough to suppress the hadronic component of the cosmic rays [3]. The isotopes that merit attention have lifetimes exceeding a few tens of days, since shorter-lived nuclei can be eliminated just by storing the detectors in the underground site for some reasonable time before starting data taking.

The cosmogenic products that have the most noticeable effect on the low-energy spectrum recorded in germanium detectors are those that decay via electronic capture (EC). The capture is often followed by the emission of a K-shell X-ray with characteristic energy between 4 and 11 keV. L- and M-shell captures will produce weaker lines at approximately 1 and 0.1 keV, respectively. The sharp line shapes and known K:L:M intensity ratios can be used to identify and subtract the associated events. However, it is preferable to reduce their initial intensities to the lowest possible level. Measurements of the production rates of EC-decaying isotopes is helpful in designing a detector-production procedure that limits these backgrounds to acceptable levels, and, more generally, to constrain models predicting the production rates of all isotopes, including those that may prove to elude direct measurements.

Another type of background of particular interest is the beta decay of tritium (^{3}H) originated from nuclear reactions induced by the interaction of the hadronic component of cosmic rays with atoms in the material [4]. The electron emitted in the beta decay of tritium has an end point Q_β of only 18.6 keV, and thus contributes to the background of low-energy events over the entire energy range relevant for low-mass WIMP searches. The lifetime of ^{3}H is particularly long ($\tau = 17.79$ y), so the tritium activity can essentially be expected to remain almost the same throughout the life of the detector. The only way to reduce this background is to limit the exposure of the crystal between the time it is grown and its installation underground. There are large uncertainties in model predictions for the production rate of ^{3}H, and available measurements can only provide crude upper limits [5].

The EDELWEISS collaboration has operated an array of 24 germanium heat-and-ionization detectors with the objective to perform searches for WIMPs with a total exposure close to 3000 kg·d, and more specific searches for low-mass WIMPs with a subset of its detectors with the best experimental energy thresholds [6]. The experiment is located in the Laboratoire Souterrain de Modane (LSM) and protected by a mean rock overburden of 1800 m (4800 m.w.e.) that reduces the cosmic ray flux to about 5 μ/m^2/day [7], i.e. 10^6 times less than at the surface. The detectors are covered by inter-

3

leaved electrodes that provide an efficient tool to reject surface events (i.e. particle interactions taking place within ∼2 mm from the detector surface) down to energies of ∼1 keV [6]. The resolutions achieved with these detectors, the reduction of the external gamma-ray background and the excellent surface-event rejection performance of the interleaved electrodes [8], have made possible a precise measurement of decay rates of different nuclei in the bulk volume of germanium detectors, and in particular, for the first time, to measure unambiguously the intensity of the tritium spectrum. Efforts were made to keep to a minimum the exposure of each crystal to cosmic rays throughout the detector production. A history of the key steps in the detector production process is available. Despite this, there are non-negligible systematic uncertainties in the recorded history of exposure times. However, these uncertainties can be tested, because unforeseen production delays[4] led to a relatively large spread (up to a factor of 4) in the exposures of the different detectors to cosmic rays. It was therefore possible to check on isotopes with the largest statistics that the observed activation rates scaled with the expectations from the recorded history of exposure times.

In the following, we detail the EDELWEISS-III setup relevant to this measurement (Section 2), as well as the data selection (Section 3). We present the expected properties of the activation of tritium and other isotopes and of the energy spectrum of the emitted electrons, and describe the analysis used to extract their intensities from the data (Section 4). These results are then converted into production rates during the exposure above ground (Section 5) and compared to a previous measurement and calculations (Section 6).

2. Experimental setup

The active target of the EDELWEISS-III WIMP search experiment consists of twenty-four 800-g *Fully-InterDigit* (FID) germanium detectors, cooled down to an operating temperature of 18 mK. All materials surrounding the detectors have been tested for their radiopurity [10]. The cryostat is surrounded by 20 cm of lead and 50 cm of polyethylene shielding. A constant flow of de-radonized air in the vicinity of the cryostat reduces the radon level down to 30 mBq/m^3. The shielding is surrounded by a 100 m^2 muon veto

---

[4] These delays occurred to solve problems related to surface current leakage, as described in [9].

made of plastic scintillator modules with a geometrical coverage of more than 98% [7].

The detectors are high-purity germanium cylindrical crystals of 70 mm in diameter and 40 mm in height. All surfaces are entirely covered with interleaved Al electrodes, biased at alternate values of potentials. The electrodes are 150 μm in width and separated by 2 mm. The potentials applied to the electrodes are chosen to determine an axial electric field in the bulk of the detector [8], while in the volume within about 2 mm from the surfaces the electric field is parallel to them. As a consequence, electron-hole pairs created in the bulk volume are collected in the axial field by the fiducial electrodes on both sides of the detector, while surface events will be collected by adjacent electrodes. This scheme extends also to the cylindrical surfaces. Fiducial (or bulk) events can thus be selected on the basis of the presence of signals of opposite signs on the fiducial electrodes on each side of the detector, and on the absence of signals on all other electrodes. The fiducial ionization E_{fid} is defined as the average of the signals on the two fiducial electrodes. Calibrations with a ^{210}Pb source in equilibrium with its Bi and Po daughters have shown that this technique can reject surface β's, α's and ^{206}Pb recoils with an efficiency of the order of 99.999% [11].

Nuclear recoils are identified by comparing the ionization signal with the $\sim \mu K$ rise in temperature accompanying each interaction, measured with two 15 mm^3 germanium NTD (Neutron Transmutation Doped) thermistors glued on each side of the detector. The charge and temperature signals are calibrated using a ^{133}Ba γ-ray source: the units of both signals are thus in keV-electron-equivalent (keV$_{ee}$). Since this work is devoted to the study of bulk electron recoil populations, the subscript ee will be omitted in the following. The signals on both thermistors are combined into a single heat measurement E_c.

The average dispersion in ionization signals E_{fid} at 0 keV is characterized by $\sigma_{fid} = 230$ eV (baseline resolution). For the heat signal E_c, the corresponding values of σ_c range from 150 to 500 eV depending on detectors. The resolution increases with the energy of the signal, with a linear term that is dominated by charge trapping effects [12]. At 356 keV, the resolutions $\sigma(E)$ are larger than the baseline σ_{fid} and σ_c values and are approximately 4 keV.

The data acquisition triggers if the amplitude of one of the heat signals

is above a threshold value[5]. These values are automatically adjusted every minute for each heat sensor according to the event rates recorded minute by minute. This, together with the 0.5 kHz sampling of the heat channels, results in the possibility to set the thresholds to levels that are close to $\sim 4.5\sigma_c$, while keeping the trigger rates per detector at approximately 50 mHz.

3. Data selection

3.1. Data set and detector selection

The data was recorded over a period of 280 calendar days, from July 2014 to April 2015. During that period, 160 days were devoted to WIMP searches. All twenty-four detectors were used to define coincidences between detectors. The average heat trigger threshold and baseline resolutions were monitored hour by hour. For this analysis, only hours when this trigger threshold is below 2 keV were selected. The hourly fiducial baseline resolution on the fiducial ionization measurement was also required to be less than 400 eV. Two detectors with a failing ionization channel, preventing an efficient application of the fiducial cut, were excluded from this exposure. Three detectors had less than one day of running time with an online threshold of below 2 keV and were also excluded from further analysis. The dead-time corrected exposure of the remaining 19 detectors is 1853 detector·day. This exposure is considered for different global fits used in order to evaluate systematic uncertainties. As each detector had a different history of exposure to cosmic rays, the final results will be based on the fits to individual detector data for the 13 detectors with individual exposure greater than 60 days, corresponding to 87.0% of the total exposure.

Similarly, a sub-sample of events with an online threshold below 0.8 keV is also defined, for precision tests of the efficiency correction and of the sample purity at energies lower than used in the final analysis. This sample corresponds to 499 detector·day, to which 10 detectors contribute.

---

[5]The online filtering on the heat signals is less efficient than the offline version, resulting in a slight degradation of resolution. Here, E_c and σ_c refer to the offline-filtered heat signals. As the trigger is applied to the signals calculated online, some E_c values may be less than their corresponding online trigger threshold by as much as σ_c.

3.2. Event selection

An event is included in the analysis if its E_{fid} (E_c) value is larger than $3.5\sigma_{fid}$ ($3\sigma_c$). The values of σ_{fid} and σ_c are measured hour by hour from Gaussian fits to the distribution of amplitudes observed in events that have not triggered the online threshold. Cuts are also performed on the χ^2 of the fit of template pulse shapes to the ionization signals, resulting in an efficiency loss of less than 1%.

Fig. 1a) shows the distribution of the fiducial ionization E_{fid} as a function of the heat signal E_c for selected events in a sample where the cut on E_{fid} has been relaxed from $3.5\sigma_{fid}$ to $3\sigma_{fid}$. On this figure, events in gray are those rejected by the fiducial cut. Namely, events are considered as having occurred in the fiducial volume if the signals on the two non-fiducial electrodes, as well as the difference between the two fiducial electrodes, are each consistent with noise within $\pm2.574\sigma$ (99%). The rejected events are mostly distributed along the two dashed lines on Fig. 1a) representing the expected location for surface beta events (blue dotted line) and surface gamma events (red dotted line). Fig. 1b) shows the same distribution after the above-described selection of fiducial events. The events in gray are those where the values of E_{fid} and E_c are not consistent with each other within 2.574σ of the experimental resolutions. They are associated with the background of heat-only events discussed in Ref. [6]. Their origin is illustrated in Figs. 1c) and d), where the low-energy part is shown together with events selected with cuts calculated using $|E_{fid}|$ instead of E_{fid}, namely, $|E_{fid}| > 3\sigma_{fid}$ and the consistency cut is applied on $(E_c - |E_{fid}|)$. For clarity, events with trigger threshold below 0.8 keV (Fig. 1c) are shown separately from those with trigger thresholds between 0.8 and 1.5 keV (Fig. 1d). The distribution of E_{fid} for heat-only events is a Gaussian centered at $E_{fid} = 0$. In Figs. 1c) and d), what is therefore observed after the rejection of events with $|E_{fid}| < 3\sigma_{fid}$ are two populations of events, symmetric in $\pm$ E_{fid}. A leakage from the population of surface gamma and beta events would be centered around the red and blue dotted lines, respectively, on Fig. 1c) and d), and not distributed symmetrically at $\pm E_{fid}$. Such a symmetry is clearly observed for the events in gray, corresponding to those rejected by the consistent cut on $E_c - |E_{fid}|$. Most of the potential backgrounds below 2 keV thus comes from heat-only events. The population of heat-only events with $E_{fid} > 0$ that are not rejected by the consistency cut will be estimated by mirroring the equivalent population with $E_{fid} < 0$. For instance, in Fig. 1c) and for $E_c <0.8$ keV, the population of gray points with $E_{fid} < 0$ is nearly equal to those with $E_{fid} > 0$. This is also true for the

events in black, indicating that most events with positive ionization energies and E_c values below 0.8 keV remaining after applying the consistency cut are due to the tail of heat-only events. Figure 1c) suggests that subtracting a sideband corresponding to events with $E_{fid} < 0$ should confirm the clear observation of the peak of events at $\sim$1.2 keV due to the capture of L-shell electrons in Ga, Ge and Zn atoms (Table 1). The efficiency of the entire analysis procedure at low energies has been tested (see Section 4.5) by comparing the L/K intensity ratio obtained with the known theoretical values, in the data sample with an online trigger threshold below 0.8 keV. It can also be observed on Fig. 1c) that the 1.2 keV peak may extend to the red dashed line corresponding to surface gamma events. This effect will be taken into account when calculating the energy dependence of the efficiency in Section 3.4. It can also be observed from Fig. 1 that the background above 2 keV is expected to be very small.

3.3. Selection of multiple-hit events

As can be deduced from the electron capture decay data listed in Table 1, events associated with ^{49}V, ^{55}Fe, ^{68}Ga and ^{68}Ge are expected to produce an L- or K-shell energy deposit in a single FID detector. The 18.6 keV electron emitted in the beta decay of tritium is also expected not to escape the fiducial volume of the detector where it occurs. Backgrounds unrelated to these decays can be reduced by rejecting events where more than one detector have triggered simultaneously. An event is considered as a single if no other detectors have triggered within an interval of 10 ms, or if the sum of the ionization energies of all other detectors having triggered in this interval is less than 1 keV.

However, Table 1 also shows that events associated with ^{65}Zn (and ^{54}Mn) are accompanied by the emission of a γ ray with an energy of 1115.5 keV (834.9 keV) with a branching ratio of 50.0% (100%). This γ ray (or internal conversion electron) may be detected simultaneously in the same detector, in which case no L- or K-shell peaks are observed. A high-energy γ ray can also escape the FID fiducial volume and be detected in one of the 23 other detectors. Thus, some of the ^{54}Mn and ^{65}Zn decays are associated with coincident events. As a result, the line intensity for these events will be obtained by a simultaneous fit of the spectra of single- and multiple-hit events. In addition, the intensity for ^{65}Zn will be corrected for the fraction of unobserved events at 8.98 keV due to the absorption of the 1115.5 keV γ-ray inside the detector itself, as estimated by Monte Carlo simulation, accounting

8

for $25\pm1\%$ of all ^{65}Zn decays. The ^{54}Mn line is included in the peak model, but its intensity is too weak to extract a reliable rate.

3.4. Energy spectrum

The energy of an event is taken as the average of E_c and E_{fid} weighted by the inverse of the square of their associated baseline resolutions σ_c and σ_{fid}, as measured hour-by-hour. A side-band spectrum corresponding to the contribution of heat-only events, obtained by replacing E_{fid} by $-E_{fid}$ in the weighted average, as described in Section 3.2, has been subtracted from the resulting spectrum. The spectrum is then corrected for the energy dependence of the efficiency due to *i)* the fiducial volume cut, *ii)* the cut on $E_{fid} > 3.5\sigma_{fid}$, and *iii)* the online trigger threshold on the heat energy[6]. The fiducial mass value per detector [6] is measured with the K-line intensities, and thus effectively includes an inefficiency due to the rejection of events where the apparent signal on a given electrode comes from a gaussian fluctuation of its baseline noise. As the energy of the event approaches zero keV, the expected signal on the non-fiducial electrodes for surface events becomes smaller than the baseline noise, and the fiducial cut can no longer reject them. The selected volume becomes the entire detector, and the effective volume increases from 70% to 100% of the detector. Fig. 1c) and d) hint at the presence of this effect as the distribution of events around the peak at 1.2 keV extends out to the line where surface gamma rays are expected. This energy dependence is calculated using the measured baseline resolutions on the signal on the non-fiducial electrodes and on the difference between those on the two fiducial electrodes. This efficiency correction is applied to the detector energy spectra, but as a convention, the fiducial exposures in all the following will be quoted for a γ ray of 10 keV. The energy-dependence of the efficiency induced by the $3.5\sigma_{fid}$ cut on E_{fid} and the online heat threshold have been calculated for each detector using the hour-by-hour measurements of both values, and taking into account the smearing effect due to the difference between the online and offline reconstruction of E_c.

The calculated corrections are very close to 1 over the entire energy range down to the analysis threshold, set at 2 keV. The validity of these corrections are thoroughly tested by applying them to the sample of events where

---

[6] The cut on $E_c > 3\sigma_c$ has a negligible effect on the efficiency once the effect of the online trigger threshold is taken into account.

9

the online threshold is below 0.8 keV. The test consists of a comparison of the measured and theoretical L/K intensity ratio for this data sample. The model predicts that the L/K efficiency ratio varies from 0.92 to 1.01 between 1.1 and 1.3 keV (the energies of the L-shell lines for ^{65}Zn and ^{68}Ge, respectively: see Table 1).

The resulting efficiency-corrected spectrum for the 1853 detector·day sample is shown in Fig. 2. The inset shows the efficiency-corrected spectrum for the data set with an online trigger threshold below 0.8 keV (499 detector·day), used to test the efficiency model and the heat-only sideband correction down to 1 keV. The electron capture and the tritium beta-decay intensities described below are taken from the fit of the sample of events with the 2 keV threshold cut.

4. Decay rate measurements

The decay rates of the different cosmogenically produced isotopes are obtained from simultaneous fits of the energy spectra of single and multiple hit events, as defined in Section 3.3. The fit is first applied to the co-added spectra of Fig. 2 in order to test its validity and estimate global systematics, and then to individual detector spectra in order to obtain individual count rates per kilogram and per day for each of the isotopes of interest. The fit model has three components: *i)* the tritium spectrum, *ii)* a Compton background and *iii)* K- and L- spectral lines.

4.1. Tritium beta spectrum

The energy spectrum of emitted electrons has an end-point value of $Q_\beta = 18.6$ keV. It is described by [13]:

$$\frac{dN}{dt} \propto \sqrt{T^2 + 2mc^2 T} \; (T + mc^2) \; (Q_\beta - T)^2 \; F(T, Z = 2) \tag{1}$$

where T is the kinetic energy, m is the mass of the electron, c the speed of light and $F(T, Z = 2)$ is the Fermi function for tritium decay. This function can be approximated in the non-relativistic limit as $x/(1 - e^{-x})$, where $x = \frac{4\pi\alpha c}{v}$, α is the fine structure constant and v is the electron velocity. With this Fermi function, and T expressed in keV, the spectral shape becomes:

$$\frac{dN}{dt} \propto (T + mc^2) \; (Q_\beta - T)^2 \; (1 - e^{-\frac{1.466}{\sqrt{T}}})^{-1} \tag{2}$$

10

This function is used to describe the tritium component in the fit. The tritium intensity is taken as the integral of the fitted component from zero to 18.6 keV. The spectral shape of Eq. (2) was not smeared with the detector-dependent energy resolutions, as it was verified that this procedure has an impact only below the analysis threshold, and in a region around the end point that has a negligible statistical weight in the determination of the intensity.

4.2. Compton background

All the peaks visible below 12 keV on Fig. 2 are due to the electron capture decays of different isotopes (mainly Ge, Ga and Zn, see Table 1) that will be detailed in Section 4.3. Between 20 and 50 keV, the Compton background is constant within statistical errors, with an average of 0.090 ± 0.002 counts/kg/day/keV. Studies of the Compton plateau below 50 keV in ^{133}Ba calibrations and GEANT4 Monte Carlo simulations also indicate that this flat behavior between 20 and 50 keV does not hint to a possible slope below 20 keV. Nevertheless, variations as much as $\sim 10\%$ of the Compton rate between 0 and 20 keV cannot be excluded, but a similar slope should also be present in multiple-hit events. The energy spectrum of multiple-hit events is also shown on Fig. 2. Apart from the expected contributions of the ^{65}Zn and, possibly, ^{54}Mn peaks (discussed below), the spectrum between 2 and 50 keV appears to be relatively consistent with a flat Compton plateau. The statistical significance of this sample is sufficient to provide an alternative template for the shape of this background. It can be noted that rejecting multiple events reduces the Compton background by almost a factor of two while having no effect on tritium decays.

In the following, the tritium and EC line intensities are obtained from a fit that includes a flat Compton background. As the fitted tritium intensity is somewhat more sensitive to the assumed shape of the Compton continuum, a systematic uncertainty is taken into account as the difference between this result and the intensity obtained with different background assumptions, namely *i)* a first order polynomial and *ii)* the multiple-hit spectrum scaled by the ratio of the number of counts between 20 and 40 keV in the single and multiple-hit spectra. The first test is performed for each individual detector. The second test requires more statistics and is only applied to the spectrum of Fig. 2.

4.3. Electron capture lines

The model for the peaks in the spectrum is not only important for getting the EC decay intensities but also to constrain the amplitude of the underlying tritium component. The structure of peaks considered in the fit is the following. The energy-dependent width of a peak is given by $\sigma(E) = \sqrt{\sigma_0^2 + (\alpha E)^2}$, where α is a free parameter and σ_0 is fixed to the value derived from the measured average baseline resolutions σ_{fid} and σ_c: $\sigma_0 = 1/\sqrt{\sigma_{fid}^{-2} + \sigma_c^{-2}}$. The global energy scale is also a free parameter of the fit.

Table 1 lists all the electron capture (EC) decays with $t_{1/2} > 10$ days, and their daughter decays, for $21 \leq Z \leq 33$. All these can potentially lead to peaks at the K-shell binding energy E_K in a germanium detector. The detectors are fully efficient to electrons, positrons and all forms of radiation down to a few eV. The energies of all prompt (< 1 ms) cascades of radiation are summed up into the same event, so only pure EC decays can produce a peak at energy E_K. By applying the fiducial selection, we ensure that the radiation is emitted at least a few millimeters below the detector surface, and only γ rays with energies above some hundred keV can escape from being summed up with the X-ray energies.

Since the detectors have been installed at LSM between 6 and 18 months before the run start in July 2014, only isotopes with half-lives longer than 100 days need to be considered. An exception is ^{71}Ge. This nucleus has a half-life of 11 days, but it is produced by (n, γ) absorption when the detector is exposed to a neutron source. This decay produces a peak at the same energy $E_K = 10.37$ keV as the EC decay of ^{68}Ge. Consequently, some care must be taken to exclude data following neutron calibrations when extracting the ^{68}Ge line intensity.

The EC decay of ^{68}Ge produces a daughter with a half-life $t_{1/2} = 67.7$ min, ^{68}Ga, that can also undergo an EC decay to ^{68}Zn with a line at $E_K = 9.66$ keV with a branching ratio of 11.12%. This value should correspond to the ratio of the peak intensities from ^{68}Ga and ^{68}Ge EC decays.

Other observable peaks should be those at the E_K values of the EC decay of ^{65}Zn, ^{55}Fe, ^{54}Mn and ^{49}V. Therefore, peaks at those energies are included in the fit, together with those at 9.66 and 10.37 keV. No peak associated to the EC decay of ^{57}Co is expected to be observed at $E_K = 7.11$ keV in our detectors, since this decay is accompanied with 122 and 136 keV γ-rays that are easily absorbed inside the fiducial volume and the ~ 2 mm layer of Ge that surrounds it. The same is true for ^{44}Ti decays, unobservable in

the fiducial volume of the detector because of the accompanying 78.3 and 67.9 keV transitions. However, the EC decay of its daughter ^{44}Sc, with a half-life $t_{1/2} = 4.0$ h, is in principle observable at $E_K = 4.04$ keV, as the accompanying 1157.0 keV γ-ray may escape detection inside the detector. The total spectrum of Fig. 2 was fitted including peaks at $E_K = 4.04$ and 7.11 keV. The resulting intensities were consistent with zero within their statistical uncertainties, and had no significant impact on the fitted tritium intensities. The heights of these two peaks have been fixed to zero for all subsequent fits.

The L-shell peak structure only needs to be included in the fit of the data sample with the <0.8 keV online threshold requirement (inset of Fig. 2). This multiplet structure is included in the fit as peaks at 1.10, 1.19 and 1.30 keV (Table 1) with intensities taken as those of the peaks at 8.98, 9.66 and 10.37 keV scaled by the same L/K ratio, which is a free parameter of the fit.

4.4. Fit to the spectra and uncertainties

The simultaneous fit to the single- and multiple-hit data shown in Fig. 2 have relatively good $\chi^2/d.o.f.$ values (1.12 and 1.03 for the fit to the data with an online trigger threshold below 2 and 0.8 keV, respectively). The fitted number of tritium counts varies by 1% whether the Compton background is assumed to be flat or to be a first order polynomial. Changing the binning of the data has a similar effect. A larger difference appears if the Compton shape is taken from that of the multiple-hit spectra instead of being assumed to be flat. In this case the fitted number of tritium counts decreases by 11%. This value is considered as a systematic uncertainty of the fitted tritium intensity associated with the uncertainty in the shape of the Compton background spectrum at low energy.

The fitted L/K ratio of the intensities of the peaks shown in the inset of Fig. 2 is 0.113 ± 0.008 (statistical error only), and agrees well with the theoretical value of 0.11 [14]. It can also be interpreted that the efficiency correction recovers at least 93% (90% C.L.) of the full efficiency at an energy of 1.25 keV, combination of the three E_L peaks of Table 1. The efficiency model described in Section 3.4 is more robust for energies above 2.0 keV, as turning on or off entirely each of the three elements in the efficiency model changes the fitted tritium intensity by less than 2%. The associated systematics is neglected as it is much smaller than the 11% uncertainty described in the previous paragraph.

4.5. Activity measurements

The fit of the entire 2 keV threshold data set results in an observed tritium activity of 0.94 ± 0.06 (stat.) ± 0.10 (syst.) events per day and per detector, extrapolated down to 0 keV using Eq. (2). However, the rate can be expected to vary from detector to detector. The fit is therefore performed for each detector individually. The tritium rate is obtained from the fit with the flat Compton background. The systematic uncertainty associated with the Compton shape is taken as the quadratic sum of the common 11% contribution discussed in the previous section and the difference between the fitted value with the flat and linear Compton backgrounds in individual detectors. The same systematic tests applied to the peak intensities showed that they are not significantly affected by uncertainties in the shape of the Compton background.

The ^{68}Ge rate is obtained from a fit that excludes the 90 days following the calibration of the detector with an AmBe neutron source. Fig. 3 shows that this cut should essentially remove all contaminations of the ^{68}Ge peak by ^{71}Ge decays. The ^{68}Ga/^{68}Ge ratio derived from the data outside this interval is 0.117 ± 0.006 and is compatible with the value of 0.1112 from Table 1.

Fig. 3 also shows that the decay rates of the ^{68,71}Ge and ^{65}Zn decrease with the proper time constant, while the tritium rate is constant, as expected from its very long half-life. As the total length of the data taking period is close to one year, the decay rate of isotopes with half-lives $t_{1/2} < 3$ y can not be considered constant. Then, the activity of an isotope with lifetime $\tau = t_{1/2}/\ln 2$ has been obtained from a fit where each event is weighted by $\exp(\frac{t-t_{ref}}{\tau})$, where t_{ref} corresponds to the middle of the data-taking period, i.e. October 30th, 2014. The fitted activity is thus the activity on this date.

The resulting decay rates per detector are listed in Table 2. The measured rates are expressed in terms of events per kilogram and per day, using the specific fiducial mass of each detector. The activities for ^{65}Zn are calculated including the count rates observed in both single- and multiple-hit events (see Section 3.3) and they are corrected for the effect of the 1115.5 keV gamma to obtain total activities. Monte Carlo simulations have shown that the probability for this gamma to escape the fiducial volume without interacting is 50.1%. Given the 50.0% branching ratio for the emission of this gamma, it can be estimated that 25% of all ^{65}Zn EC decays do not produce a visible 8.98 keV peak, and the observed rate is corrected accordingly.

5. Exposure history

The population of cosmogenically produced radioactive isotopes in germanium is expected to be reduced to a negligible level during the crystallization process, except for ^{68}Ge. The activation occurs while the crystal is stored above ground, induced mostly by high-energy neutron interactions. After a time $\Delta t = t - t_g$ after crystal growth happening at time t_g, the isotope activity per unit mass $a(t)$ increases as:

$$a(t) = a_{max} \left(1 - e^{-\frac{t - t_g}{\tau}}\right) \tag{3}$$

where a_{max} is the maximal activation, obtained when it becomes equal to the production rate, and τ is the lifetime. The value of a_{max} for a given isotope depends on the flux of cosmic rays and the cross section for its production (including decay chains). Once the detector is shielded from cosmic rays by a significant thickness of rock so further activation can be neglected, the decay rate changes as:

$$a(t) = a_{max} \left(1 - e^{-\frac{t_s - t_g}{\tau}}\right) e^{-\frac{t - t_s}{\tau}} \tag{4}$$

where t_s is the time at which the detector is screened from cosmic rays. A precise history detailing the succession and the length of the periods of time during which the detector is exposed or protected from cosmic rays is thus essential to evaluate isotope activities at a given time.

The crystals have been produced gradually from September 2011 to December 2012, and they have been installed at the LSM in three batches: in January 2013, in September 2013 and in January 2014. The time periods of exposure to cosmic rays and underground storage of the Ge detectors are listed per detector in Table 3. The germanium crystals were first exposed above ground in a period t_{exp1} starting from their production by UMICORE in Belgium, during their polishing at BSI in Latvia, up to their shipment to different shallow underground sites at CEA in France. The shallow sites were at least 10 m.w.e. deep. Considering the attenuation length of the neutron flux of 148 g/cm^2 [15], such depths result in a reduction of activation by a factor 850. Cosmogenic production during the time t_{dec1} when the crystals were stored in the shallow sites is therefore neglected. The second exposure time t_{exp2} occurs when the detector is shipped from the shallow sites to the nearby laboratories of CSNSM and CEA, where electrodes are evaporated, the surfaces are etched with XeF$_2$ [9], the NTD heat sensors are glued to them, and the detectors are shipped to an underground site. This site is

either the LSM, or, for three of the detectors, one of the shallow sites, where they were stored prior to a grouped shipment to LSM. The last decay period t_{dec2} corresponds to the interval between their arrival at LSM and the date of October 30th, 2014 (t_{ref}). For the three detectors stored in the shallow site before their shipment to LSM, this period is included in t_{dec2}, and the short shipment time is included in the systematic uncertainty.

Confirmed dates are those of the crystal production, the end of their polishing, the start and end of the electrode evaporation, the XeF_2 etching processes, the glueing of the NTD, and of their arrival at the LSM underground laboratory. Tracking of detector shipments and in-and-out of the shallow sites are not documented as precisely. This is taken into account by ascribing a ± 7 day uncertainty on the duration of each shipment, resulting in the systematic uncertainty shown in Table 3. This uncertainty is anti-correlated between two consecutive periods. The time periods t_{exp1} and t_{dec2} are bound by only one transport, and therefore have a smaller uncertainty. For two of the detectors, FID827 and FID828, there is a significantly larger uncertainty on the time interval between detector fabrication and shipment to underground site.

Considering the succession of exposure times (t_{exp1} and t_{exp2}) and cooling-off periods (t_{dec1} and t_{dec2}), and using Eqs. (3) and (4) the decay rate observed on October 30th, 2014 (t_{ref}) in a detector ($\frac{dN}{dt}$) is related to the production rate (P) by:

$$\frac{dN}{dt} = P \times [(1 - e^{\frac{-t_{exp1}}{\tau}})(e^{\frac{-(t_{dec1} + t_{exp2} + t_{dec2})}{\tau}}) + (1 - e^{\frac{-t_{exp2}}{\tau}})(e^{\frac{-t_{dec2}}{\tau}})] \quad (5)$$

The expression in brackets in Eq. (5) corresponds to the saturation fraction $f_s(t_{ref})$, i.e. the activation at the time t_{ref} expressed as a fraction of a_{max}, for a given detector history. Table 4 lists f_s values calculated from Table 3, together with their systematic uncertainties $\sigma(f_s)$.

The calculation of f_s can also be done at any other time t between t_g and t_{ref}. This is what is shown on Fig. 4 for ^{65}Zn (top) and ^{3}H (bottom), for the two detectors FID844 (left) and FID827 (right). The time axis starts at crystallization and ends on the reference day t_{ref}. The red lines correspond to the history described in Table 3, while the blue dotted lines are calculated using the $\pm 1\sigma$ uncertainties. The detector FID844 has a standard history, where the two exposures t_{exp1} and t_{exp2} are separated by a relatively long cooling-down period t_{dec1}. This period is sufficiently long compared to the mean lifetime of ^{65}Zn that the activity at t_{ref} is dominated by the effect

16

of the last exposure t_{exp2}, and consequently the uncertainty on $f_s(t_{ref})$ is dominated by that on t_{exp2}. This is not the case for ^{3}H ($t_{dec1} \ll \tau$), where both exposure times t_{exp1} and t_{exp2} contribute equally to $f_s(t_{ref})$. FID827 is an example of a different history, where t_{dec1} is also small compared to the ^{65}Zn lifetime.

As a first consistency test of the detector history model with the observed count rates, the correlation factor between the measured rate and the saturation fraction of ^{68}Ge and ^{65}Zn, for which measurements provide higher statistics, were evaluated. The correlation factors, calculated as Pearson product-moment correlation coefficient, are 0.90 and 0.83, respectively. This is a good indication that the observed count rate variations from detector to detector are indeed caused by the known history differences between them. In the final analysis (next section), the validity of this correlation is tested taking into account the uncertainties of the measurements and detector history.

6. Production rates

6.1. Experimental Results

Figures 5 to 9 show the measured decay rates of Table 2, as a function of the saturation fraction of Table 4, for the thirteen FID detectors. Each plot corresponds to a different isotope. The data are fitted with a first degree polynomial: $y = P \cdot x$, where x is the saturation fraction, y is the measured decay rate and the coefficient P is the production rate of this particular isotope. The fits are shown by solid red lines. Errors in the count rates and saturation fraction have been taken into account. The fit parameters P corresponding to the best estimates of the production rate are listed in Table 5, together with the $\chi^2/d.o.f.$ of the fit. The final production rate values and their total errors are listed in Table 6.

Most fits result in good reduced χ^2 values, except ^{65}Zn and ^{3}H. To investigate this further, the fits were repeated with different scaling factors S applied to the systematic uncertainty in the saturation fraction. The reduced χ^2 values for ^{65}Zn and ^{3}H are equal or less than one for $S = 2$. We therefore include as an additional systematic uncertainty in the production rate of these two isotopes the difference between the results with $S = 1$ and $S = 2$. The final production rate values and their total errors are listed in Table 6.

Additional checks for consistency of the results have been carried out. Three detectors (FID826, 827 and 828) have been removed from the analysis

17

because they were stored at a shallow site after being fully assembled but before being shipped to LSM, which could induce additional uncertainty relative to other detectors that were shipped directly to LSM. Production rates per isotopes agree within statistical errors with initial results. Although no activation is assumed to occur at the shallow sites, we repeated the analysis considering an activation rate equivalent to either 2% or 5% of the value on the surface. This resulted in small changes in the saturation fraction at $t = t_{ref}$ which are within the systematic uncertainty arising from the shipment history alone.

6.2. Calculated production rates

Figures 5 to 9 also show the lines corresponding to production rate estimates from different models.

The production rate, P_i, of a radioactive isotope i can be calculated as follows:

$$P_i = \sum_j N_j \int \phi(E)\sigma_{ij}(E)dE \tag{6}$$

where N_j is the number of target nuclear isotope j, σ_{ij} is the excitation function of isotope i produced by neutrons on stable isotopes of material j, and ϕ is the cosmic neutron flux.

Estimates of the production rate have been carried out with the ACTIVIA code [16]. The code does not include proton activation of materials; the hadronic part of the cosmic-ray spectrum at the surface is dominated by neutrons [15]. The original ACTIVIA code uses the neutron energy spectrum at the surface from [15] but, as shown in Ref. [17], this spectrum does not match recent experimental data [18]. We carried out the calculations of production rates by replacing the original neutron spectrum with that from Ref. [18].

These calculations are performed using a cosmic ray neutron spectrum in the northern hemisphere parametrized as follows [18]:

$$
\begin{aligned}
\phi(E) &= 1.006 \times 10^{-6} e^{-0.35 \ln^2 E + 2.1451 \ln E} \\
&\quad + 1.011 \times 10^{-3} e^{-0.4106 \ln^2 E - 0.667 \ln E}
\end{aligned} \tag{7}
$$

where E is the neutron kinetic energy in MeV and ϕ is in units of $\mathrm{cm}^{-2}\,\mathrm{s}^{-1}\,\mathrm{MeV}^{-1}$.

We have also used semi-empirical cross sections from Refs. [19, 20, 21, 22, 23] and the cross sections from the MENDL-2P libraries [24], shown, respectively, as dashed and dash-dotted light-blue lines in Figs. 5 to 9.

The results of the calculations are listed in the third column of Table 6. They are labeled (a) or (b) if they use the semi-empirical cross sections [19, 20, 21, 22, 23] or the MENDL-2P [24] database, respectively. For ^{49}V both calculations give the same production rate. Our calculations with ACTIVIA, quoted in the second column of Table 6, show that excitation functions may account for up to a factor of 2 difference in the production rate of ^{68}Ge. The difference increases with the atomic number of the isotope produced.

Effects on the production rates caused by differences in cross sections and cosmogenic neutron energy spectra in ACTIVIA and GEANT4 codes [25] have been estimated in Ref. [17]. There, the neutron spectrum from [18] was taken as measured values for New York location whereas in the present work the parameterization [18] of these data has been used as given by Eq. (7). The two approaches (data vs parameterization of these data) differ by no more than 2%.

Comparing production rates from calculations in Ref. [26], listed in the third and fourth columns of Table 6, we can conclude that different input cosmic-ray neutron spectra, from Refs. [15] and [18], can lead to a variation in production rates of about 20-30% for the isotopes considered here.

6.3. Comparison with previous measurements and models

Different model estimates have been compared to the measurements presented in the previous sections. In Figs. 5 to 9, the EDELWEISS data and the best fit to these data are compared to the ACTIVIA calculations performed within this work considering semi-empirical [19, 20, 21, 22, 23] (dashed lightblue line) and MENDL-2P [24] (dash-dotted light-blue line) cross sections. Calculations from previous works are also shown in dashed lines: Cebrian et al. [26] (green), Klapdor-Kleingrothaus et al. [27] (blue), and Mei et al. [5] using TALYS cross sections (purple), the update of this work from Zhang et al. [17] (olive-green) and the estimates from Avignone et al. [4] (orange).

The calculations from Ref. [26] that assume Ziegler [15] and Gordon et al. [18] cosmic neutron spectra are shown as dotted and dashed-dotted lines, respectively. All these calculated rates are also listed in Table 6.

In addition, the previous experimental measurements for ^{68}Ge and ^{65}Zn reported in Ref. [4] are shown as solid orange line in Fig. 7 and Fig. 9 and appear in the last column of Table 6.

Among themselves, these models agree within a factor of 2-3 for ^{65}Zn, for ^{68}Ge and ^{55}Fe, whereas the difference for ^{3}H can be close to one order of magnitude, ranging from 27.7 to 210 nuclei/kg/day.

Ref. [5] quotes an experimental upper limit on the ^{3}H production rate of 21 nuclei/kg/day of ^{3}H from a by-eye fit to the IGEX data, in tension with an estimate of 27.7 nuclei/kg/day from the model using the TALYS cross sections and the cosmic neutron spectrum parameterization from Ref. [18]. A comparison of the latter value with most recent calculations is available in Ref. [17]. However, the tritium production rates estimated with GEANT4 (I) and ACTIVIA (II) are larger: 52.4 nuclei/kg/day and 48.3 nuclei/kg/day, respectively, and are closer to our measurement of 82±21 nuclei/kg/day with statistical and systematic uncertainties included.

The measured production rates for all nuclei are within a factor two of our ACTIVIA calculations, with preferred cross sections from MENDL-2P library, especially for the nuclei ^{65}Zn and ^{68}Ge. The closest agreement between data and our ACTIVIA calculations is for ^{55}Fe. Concerning the other calculations listed in Table 6, those predicting the largest rates are systematically favored, except for the ^{3}H prediction from Ref. [4].

The significance of the tension between our measurements and ACTIVIA calculations can be assessed by comparing the difference in their values to the quoted experimental uncertainties. The ACTIVIA estimates from this work show a 1.7σ to 1.8σ deviation from the measured production rate of ^{3}H of 82 ± 21 nuclei/kg/day. The disagreement with the prediction from Ref. [4] using the prescription from [28] is stronger, at 6σ. The agreement between the measured rates and those predicted by ACTIVIA (average value), for isotopes other than ^{3}H, is better: deviations of less than 1.7σ (statistical error only) are observed for ^{55}Fe, ^{49}V and ^{65}Zn. It should be noted that the present measurement for ^{65}Zn disagrees with that in Ref. [4] by 5.9σ (statistical error only). Including systematic uncertainty, the disagreement is still strong at a 4.8σ level.

Since the population of ^{68}Ge is not reduced to zero during the germanium crystallization, there is an uncertainty in its saturation fraction associated to the amount of time the germanium ore was exposed to cosmic rays before the crystal growing. The first value for ^{68}Ge in Table 5 (202 ± 16) is calculated assuming no exposure prior to the crystallization. The second assumes a 3-year exposure before the crystal growth, reaching a population close to saturation. In this second scenario, the production rate is reduced to 84 ± 3 nuclei/kg/day. The χ^2 of the fit is reduced from 3.2 to 1.0 assuming a scaling factor of $\sigma(f_s)$ of 2 (see Section 6.1) resulting in a production rate of 84 ± 6, from which is obtained a lower limit on the production rate of 74 nuclei/kg/day at 90% C.L.It is, nevertheless, 3.6σ above the average value of

the ACTIVA results, considering the difference between the two predictions as a systematic uncertainty. Ref. [4] reports a value of 30 ± 7 nuclei/kg/day at saturation, 6.3σ below our lower limit. The present ^{65}Zn production rate measurement is 2.8 ± 0.6 times larger than that of Ref. [4]. The lower limit on the ^{68}Ge value is also larger than the measurement in that same reference, by a similar factor of 2.5. In order to evaluate the possible source of this discrepancy, more detailed information on the analysis of the data of Ref. [4] are needed.

Our measurements, extending to more than one cosmogenic activation product, can help to improve the models by constraining them better and thus contribute to the reduction of the systematic uncertainties associated with the wide variation of their predictions. The discrepancies of predictions from nucleus to nucleus, and the significant difference in the ACTIVIA calculations with semi-empirical or MENDL-2P cross sections suggest that an important source of uncertainties in the calculations comes from the different excitation functions of an isotope produced by neutrons on the stable parent isotope of the material.

7. Conclusion

The cosmogenic activation of various isotopes in the germanium detectors of the EDELWEISS-III experiment has been measured. The data for five isotopes and thirteen detectors with different exposure times lead to a consistent set of measurements. The first measurement of the ^{3}H decay rate in germanium detectors is presented. It has been interpreted in terms of production rate of 82 ± 21 nuclei/kg/day with statistical and systematic uncertainties included. The tritium production due to cosmic-ray neutrons is thus important and the present measurement provides valuable information needed to evaluate the reduction of the exposure to cosmic rays necessary for germanium detector arrays used for dark matter searches. The measured production rates on ^{49}V, ^{55}Fe and ^{65}Zn of 2.8 ± 0.6 nuclei/kg/day, 4.6 ± 0.7 nuclei/kg/day and 106 ± 13 nuclei/kg/day, respectively, presented here are the most accurate to-date. A lower limit of 74 nuclei/kg/day at 90% C.L. on production rate of ^{68}Ge is discussed.

The measured ^{65}Zn production rate and the lower limit on that of ^{68}Ge are a factor 2.7 ± 0.6 larger than the measurements reported in Ref. [4]. The origin of this discrepancy is unknown.

The measurements agree within a factor of two with estimates performed with the ACTIVIA code within this work. The best agreement is found for ^{49}V and ^{55}Fe. The estimates for ^{3}H, ^{65}Zn and ^{68}Ge tend to underestimate the measured rates, with significance ranging from 1.7σ to 6σ. The difference between these predictions and those from other models can also differ by as much as a factor of two in most cases, with no single model giving a satisfying description for all measured isotopes. It can be foreseen that the precision of the present measurements will help constrain and further improve the models.

8. Acknowledgments

References

[1] J. L. Feng, Ann. Rev. Astron. Astrophys. **48**, 495–545 (2010).

[2] T. Shutt *et al.*, Phys. Rev. Lett. **69**, 3425–3427Dec (1992).

[3] K. Farley, J. Libarkin, S. Mukhopadhyay, and W. Amidon, Earth and Planetary Science Letters **248**, 451 – 461 (2006).

[4] F. T. Avignone III *et al.*, Nucl. Phys. B (Proc. Suppl.) **28A**, 280 – 285 (1992).

[5] D.-M. Mei, Z.-B. Yin, and S. Elliott, Astropart. Phys. **31**, 417 – 420 (2009).

[6] E. Armengaud *et al.* (EDELWEISS Collaboration), JCAP **1605**, p. 019 (2016).

[7] B. Schmidt *et al.* (EDELWEISS), Astropart. Phys. **44**, 28–39 (2013).

[8] A. Broniatowski *et al.*, Phys. Lett. **B681**, 305–309 (2009).

[9] S. Marnieros, Bergé, *et al.*, .

[10] S. Scorza (for the EDELWEISS Collaboration), AIP Conf. Proc. **1672** (2015).

[11] J. Gascon and N. Bastidon (for the EDELWEISS Collaboration), J. Low. Temp. Phys. **176**, 870–875 (2014).

[12] Q. Arnaud *et al.* (EDELWEISS Collaboration), (2016), arXiv:1606.08097 .

[13] B. Lowell and Z. Cheng-xing, Annals Phys. **249**, 298–361 (1996), arXiv:hep-ph/9511209 [hep-ph] .

[14] J. N. Bahcall, Phys. Rev. **132**, 362–367 (1963).

[15] J. F. Ziegler, IBM Journal of Research and Development **42**, 117–140 (1998).

[16] J. Back and Y. Ramachers, Nucl. Instrum. Meth. A **586**, 286 – 294 (2008).

23

[17] C. Zhang, D.-M. Mei, V. A. Kudryavtsev, and S. Fiorucci, arXiv:1603.00098 (2016).

[18] M. S. Gordon *et al.*, IEEE Trans. Nucl. Sci. **51**, 3427–3434 (2004).

[19] R. Silberberg and C. Tsao, Astrophys. J. Suppl. **220 (I)**, p. 25 (1973).

[20] R. Silberberg and C. Tsao, Astrophys. J. Suppl. **35**, p. 129 (1997).

[21] R. Silberberg, C. Tsao, and J. Letaw, Astrophys. J. Suppl. **58**, p. 873 (1985).

[22] R. Silberberg and C. Tsao, Phys. Rep. **191**, p. 351 (1990).

[23] R. Silberberg and C. Tsao, Astrophys. J. **501**, p. 911 (1998).

[24] Y. Shubin *et al.*, MENDL-2P: Proton Reaction Data Library for Nuclear Activation (Medium Energy Nuclear Data Library) **IAEA-NSD-204** (1998).

[25] S. Agostinelli *et al.*, Nucl. Instrum. Meth. A **506**, 250 – 303 (2003).

[26] S. Cebrian *et al.*, Astropart. Phys. **33**, 316 – 329 (2010).

[27] H. Klapdor-Kleingrothaus *et al.*, Nucl. Instrum. Meth. A **481**, 149 – 159 (2002).

[28] W. Hess, H. Patterson, and R. Wallace, Phys. Rev. **116**, p. 449 (1959).

[29] `http://www.nndc.bnl.gov/nudat2/` .

[30] J. A. Bearden and A. F. Burr, Rev. Mod. Phys **39**, p. 125 (1967).

Table 1: Table of electron capture (EC) decays with half-lives above 10 days for 21≤Z≤33. The half-lives and decay properties are from Ref. [29]. The binding energy of electrons in the K-shell (E_K) are from Ref. [30], as well as those for L-shell electrons that are used in the fit shown in the inset of Fig. 2.

	Daughter Isotope	E_K (keV)	E_L (keV)	Half-life $t_{1/2}$	EC B.R. (%)	Coincidences with γ rays and internal conversion
^{74}As	^{74}Ge	11.10		17.8 d	66	
^{73}As	^{73}Ge	11.10		80.3 d	100	
^{71}Ge	^{71}Ga	10.37	1.30	11.4 d	100	
^{68}Ge	^{68}Ga	10.37	1.30	271.0 d	100	
^{68}Ga	^{68}Zn	9.66	1.19	67.7 min	11.12	
^{65}Zn	^{65}Cu	8.98	1.10	243.9 d	100	50.0% (1115.5 keV)
^{58}Co	^{58}Fe	7.11		70.9 d	100	99.5% (810.8 keV)
^{57}Co	^{57}Fe	7.11		271.7 d	100	99.8% (122.1 or 136.5 keV)
^{56}Co	^{56}Fe	7.11		77.2 d	100	100% (846.8 keV and others)
^{55}Fe	^{55}Mn	6.54		2.74 y	100	
^{54}Mn	^{54}Cr	5.99		312.1 d	100	100% (834.9 keV)
^{51}Cr	^{51}V	5.46		27.7 d	100	9.9% (320.1 keV)
^{49}V	^{49}Ti	4.97		330 d	100	
^{44}Ti	^{44}Sc	4.49		60.0 y	100	100% (78.3 + 67.9 keV)
^{44}Sc	^{44}Ca	4.04		4.0 h	100	99.9% (1157.0 keV)

Table 2: Measured decay rates of different isotopes ($\frac{dN}{dt}$) along with their uncertainties ($\sigma(\frac{dN}{dt})$) per detector. Both are given in units of decays·kg^{-1}day^{-1}. In case of the ^{3}H the error on the measured rate includes statistical and systematic uncertainties. Systematic uncertainty is based on the comparison of the decay rate with the flat/inclined spectrum of Compton electrons. Measured rates of ^{65}Zn decay include 25% correction as explained in the text. All the rates have been weighted over the fiducial mass considered in the low threshold WIMP search analysis [6].

Detector	^{3}H		^{65}Zn		^{55}Fe		^{68}Ge		^{49}V	
	$\frac{dN}{dt}$	$\sigma(\frac{dN}{dt})$	$\frac{dN}{dt}$	$\sigma(\frac{dN}{dt})$	$\frac{dN}{dt}$	$\sigma(\frac{dN}{dt})$	$\frac{dN}{dt}$	$\sigma(\frac{dN}{dt})$	$\sigma(\frac{dN}{dt})$	$\sigma(\frac{dN}{dt})$
FID823	0.36	0.45	0.69	0.22	0.16	0.11	1.52	0.25	0.14	0.10
FID824	0.67	0.34	1.15	0.18	0.10	0.06	1.93	0.23	0.12	0.07
FID825	0.30	0.29	1.14	0.18	0.10	0.06	2.21	0.22	0.03	0.05
FID826	0.92	0.46	1.75	0.26	0.17	0.10	2.58	0.35	0.13	0.11
FID827	1.68	0.51	3.84	0.27	0.31	0.09	8.77	0.42	0.18	0.08
FID828	0.93	0.55	3.18	0.28	0.26	0.09	11.56	0.51	0.17	0.08
FID837	0.75	0.47	3.29	0.27	0.19	0.08	7.37	0.39	0.12	0.07
FID838	1.10	0.35	3.57	0.27	0.27	0.09	11.50	0.46	0.15	0.07
FID839	2.35	0.45	2.45	0.23	0.16	0.08	6.84	0.36	0.04	0.07
FID841	1.18	0.42	3.21	0.26	0.12	0.07	4.33	0.29	0.12	0.07
FID842	2.09	0.50	3.03	0.27	0.38	0.11	4.25	0.31	0.09	0.08
FID844	1.07	0.41	1.21	0.21	0.12	0.08	3.93	0.29	0.12	0.08
FID845	2.52	0.86	1.44	0.23	0.21	0.11	2.54	0.27	0.28	0.12

Table 3: Exposure and cool-off times in days for all detectors: t_{dec2} is calculated as the time between the day when the detector has last been moved underground and the middle of the run. Listed as Δt is the uncertainty considered in our history model due to the absence of some records.

Detector	t_{exp1}	Δt_{exp1}	t_{dec1}	Δt_{dec1}	t_{exp2}	Δt_{exp2}	t_{dec2}	Δt_{dec2}
	(days)		(days)		(days)		(days)	
FID823	47	±7	398	∓14	29	±14	1002	∓7
FID824	47	±7	404	∓14	23	±14	1002	∓7
FID825	32	±7	376	∓14	20	±14	1002	∓7
FID826	58	±7	316	∓14	21	±14	984	∓7
FID827	82	±7	110	∓14	127	±42	798	∓35
FID828	37	±7	123	∓14	119	±42	798	∓35
FID837	50	±7	394	∓14	91	±14	612	∓7
FID838	59	±7	342	∓14	88	±14	612	∓7
FID839	43	±7	347	∓14	84	±14	612	∓7
FID841	31	±7	819	∓14	45	±14	612	∓7
FID842	43	±7	821	∓14	35	±14	612	∓7
FID844	35	±7	833	∓14	31	±14	612	∓7
FID845	30	±7	831	∓14	26	±14	612	∓7

Table 4: Saturation fraction f_s along with their uncertainties, $\sigma(f_s)$, per detector.

Detector	^{3}**H**		^{65}**Zn**		^{55}**Fe**		^{68}**Ge**		^{49}**V**	
	f_s	$\sigma(f_s)$	f_s	$\sigma(f_s)$	f_s	$\sigma(f_s)$	f_s	$\sigma(f_s)$	f_s	$\sigma(f_s)$
FID823	0.0097	0.0028	0.0068	0.0026	0.0220	0.0068	0.0085	0.0032	0.0119	0.0043
FID824	0.0089	0.0028	0.0059	0.0027	0.0200	0.0068	0.0074	0.0032	0.0104	0.0043
FID825	0.0067	0.0028	0.0049	0.0028	0.0154	0.0068	0.0061	0.0033	0.0085	0.0044
FID826	0.0101	0.0028	0.0071	0.0029	0.0232	0.0070	0.0090	0.0035	0.0126	0.0046
FID827	0.0279	0.0068	0.0423	0.0131	0.0755	0.0194	0.0494	0.0150	0.0616	0.0180
FID828	0.0209	0.0068	0.0349	0.0131	0.0579	0.0194	0.0404	0.0150	0.0497	0.0180
FID837	0.0192	0.0029	0.0459	0.0072	0.0561	0.0086	0.0507	0.0080	0.0580	0.0091
FID838	0.0200	0.0029	0.0469	0.0074	0.0584	0.0087	0.0519	0.0082	0.0597	0.0093
FID839	0.0174	0.0029	0.0433	0.0074	0.0515	0.0087	0.0477	0.0082	0.0544	0.0093
FID841	0.0102	0.0029	0.0225	0.0070	0.0279	0.0082	0.0246	0.0077	0.0279	0.0086
FID842	0.0102	0.0029	0.0185	0.0071	0.0265	0.0082	0.0205	0.0078	0.0237	0.0087
FID844	0.0087	0.0029	0.0164	0.0072	0.0227	0.0082	0.0180	0.0078	0.0208	0.0087
FID845	0.0074	0.0029	0.0139	0.0072	0.0193	0.0083	0.0153	0.0078	0.0176	0.0088

Table 5: Table of production rates (fit values) considering a selection of 13 detectors. No systematics uncertainties are considered. For ^{68}Ge, a lower limit at saturation (sat) is quoted as well.

Isotope	**nuclei/kg/day**	$\chi^2/d.o.f.$
^{3}**H**	82 ± 12	1.76
^{49}**V**	2.8 ± 0.6	0.92
^{65}**Zn**	106 ± 10	2.43
^{55}**Fe**	4.6 ± 0.7	0.72
^{68}**Ge**	202 ± 16	0.93
	84 ± 3 (sat)	3.17

Table 6: Rates of production (expressed in $kg^{-1} \cdot day^{-1}$) of isotopes induced in natural germanium at sea level as measured in EDELWEISS III germanium detectors, compared with previous estimates and measurements in Ref. [26], [5], [17], [27] and [4]. Errors on the production rate include statistical and for ^{3}H and ^{65}Zn systematic uncertainties, too. Systematic uncertainty is based on the minimization of the reduced χ^2. Estimate in this work refers to ACTIVIA calculation, considering semi-empirical [19, 20, 21, 22, 23] (a) and MENDL-2P database (b) [24] cross sections. For ^{49}V, both calculations give the same result. An upper limit for ^{3}H from IGEX data (E) is shown together with calculations [5] for all isotopes. (I) and (II) refer to GEANT4 and ACTIVIA calculations from [17]. The lower limit for ^{68}Ge at saturation value is listed. It is derived from the fit value of 84 ± 6 at a 90% C.L. The last two columns refer to estimates from model [28] and experimental data (Exp.) from Ref. [4].

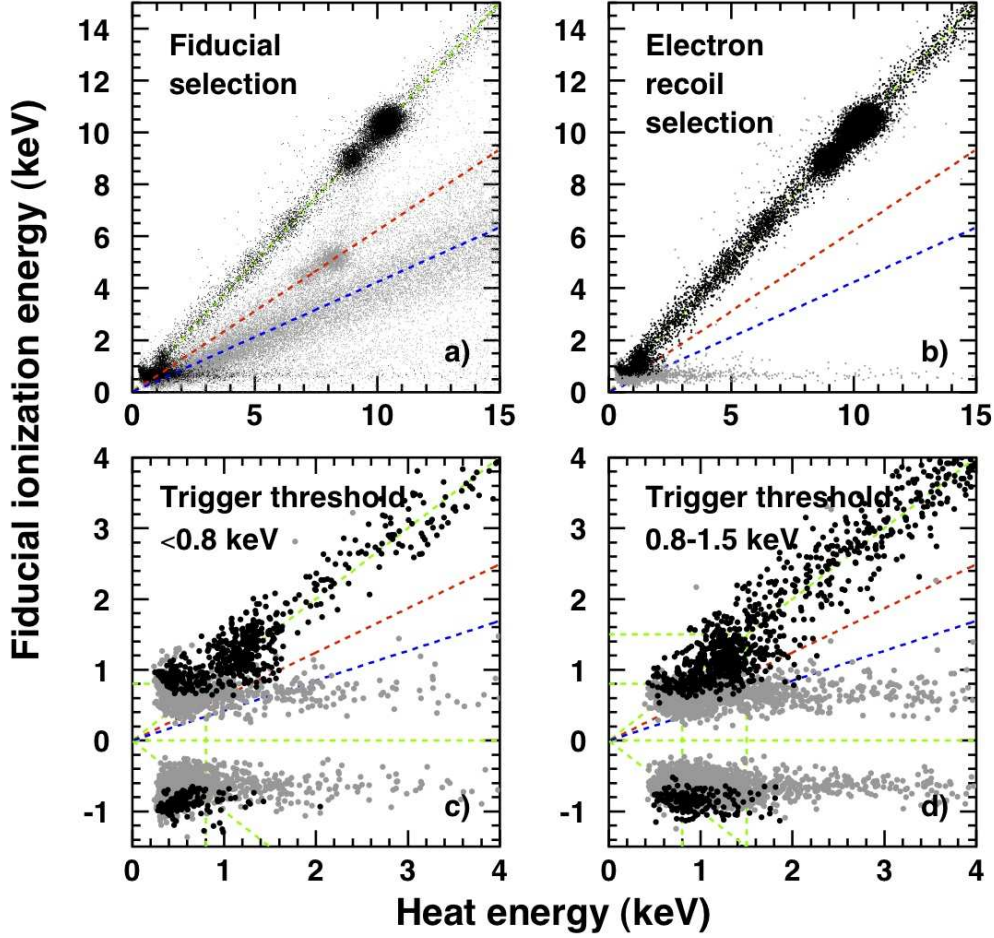|	This work		Ref. [26]		Ref. [5]	Ref. [17]	Ref. [27]	Ref. [4]	
	Exp.	Calc.	(Ziegler)	(Gordon)				From [28]	Exp.
^{3}H	82±21	46$_{(a)}$ 43.5$_{(b)}$			27.7 <21$_{(E)}$	48.3 $_{(I)}$ 52.4 $_{(II)}$		210	
^{49}V	2.8±0.6	1.9 (a,b)							
^{65}Zn	106±13	38.7$_{(a)}$ 65.8$_{(b)}$	77	63	37.1		79	34.4	38±6
^{55}Fe	4.6±0.7	3.5$_{(a)}$ 4.0$_{(b)}$	8.0	6.0	8.6		8.4		
^{68}Ge	>74	23.1$_{(a)}$ 45.0$_{(b)}$	89	60	41.3		58.4	29.6	30±7

Figure 1: Distribution of the fiducial ionization E_{fid} versus heat energy E_c at different steps of the data selection. Panel a): events passing the χ^2 selection, and having $E_c > 3\sigma_c$ and $|E_{fid}| > 3\sigma_{fid}$, where the black markers are events passing the fiducial selection, and those in gray do not pass this cut. Dotted red and blue lines represent the average ionization yields of surface gamma and surface beta events, respectively. Panel b): events after the fiducial selection, with black markers representing the events passing the $E_c - E_{fid}$ consistency cut to select fiducial electron recoils, and gray markers to represent those that do not pass this cut. Bottom panels: same as figure b), but now extended to negative ionization energies to better illustrate the contamination by heat-only events (see text). Figures c) and d) refer to events with a trigger selection on the heat signal (as measured online) below 0.8 keV, and in the range 0.8-1.5 keV, respectively.
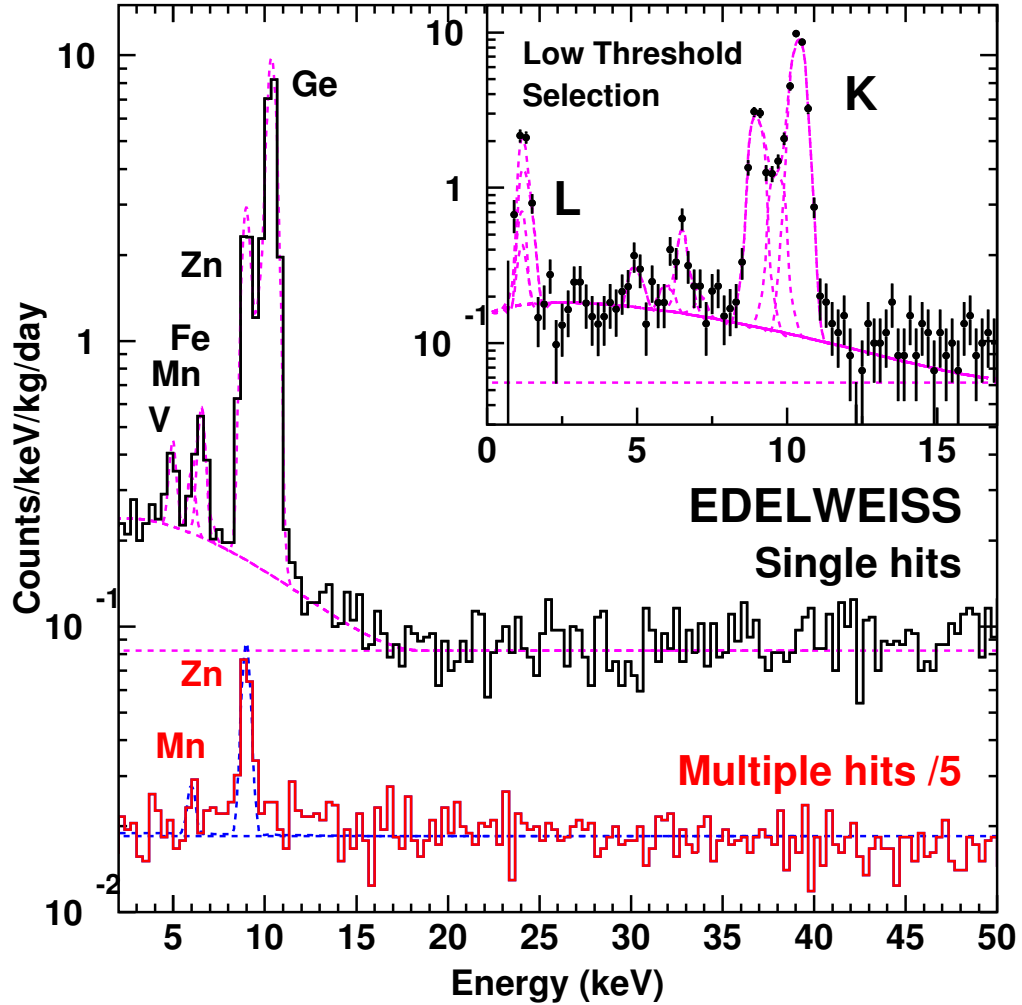
Figure 2: Efficiency-corrected spectrum for the 1853 detector·day sample, together with the fit to the data described in the text. The distribution for single events is in black, and the red spectrum representing multiple-hit events has been scaled down by a factor of 5 for clarity. The inset shows the efficiency-corrected spectrum for the 0.8 keV selection (499 detector·day), used to test down to 1 keV the efficiency model and sideband correction described in the text and in Fig. 1.
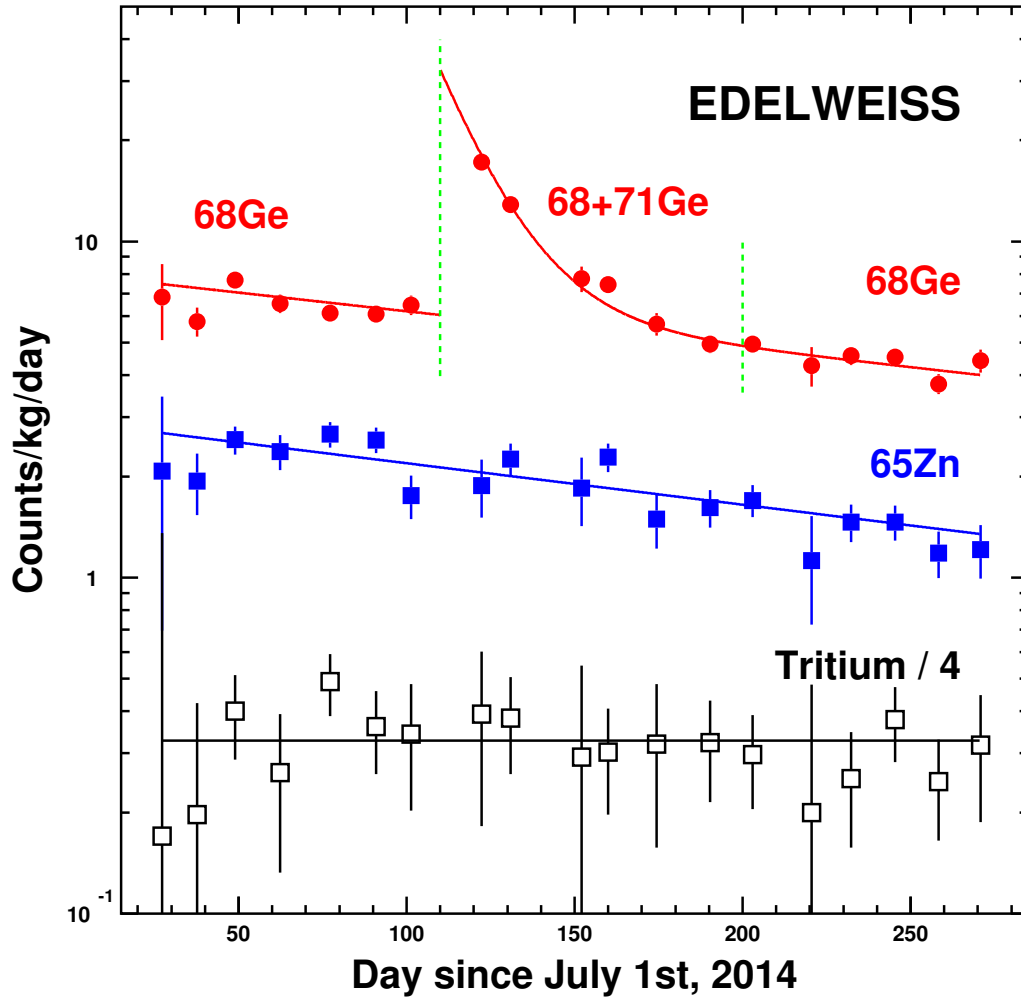
31

Figure 3: Count rates (in counts per kg·d) in the peaks at 8.98 keV (Zn) and 10.37 keV (Ge) as well as in the tritium spectrum, as a function of the time (in days since July 1st, 2014). Each rate and the average time at which it was measured is calculated in bins of 14 days, and excludes the data set taken with calibration sources. The tritium rates have been scaled by a factor 4 for clarity. The full lines are fits to the data of exponentials with the expected lifetime for each isotope. The vertical dashed lines represent the data set excluded from the ^{68}Ge rate measurement, as it is clearly affected by the neutron activation of germanium following the AmBe calibration occurring between days 108 and 112.
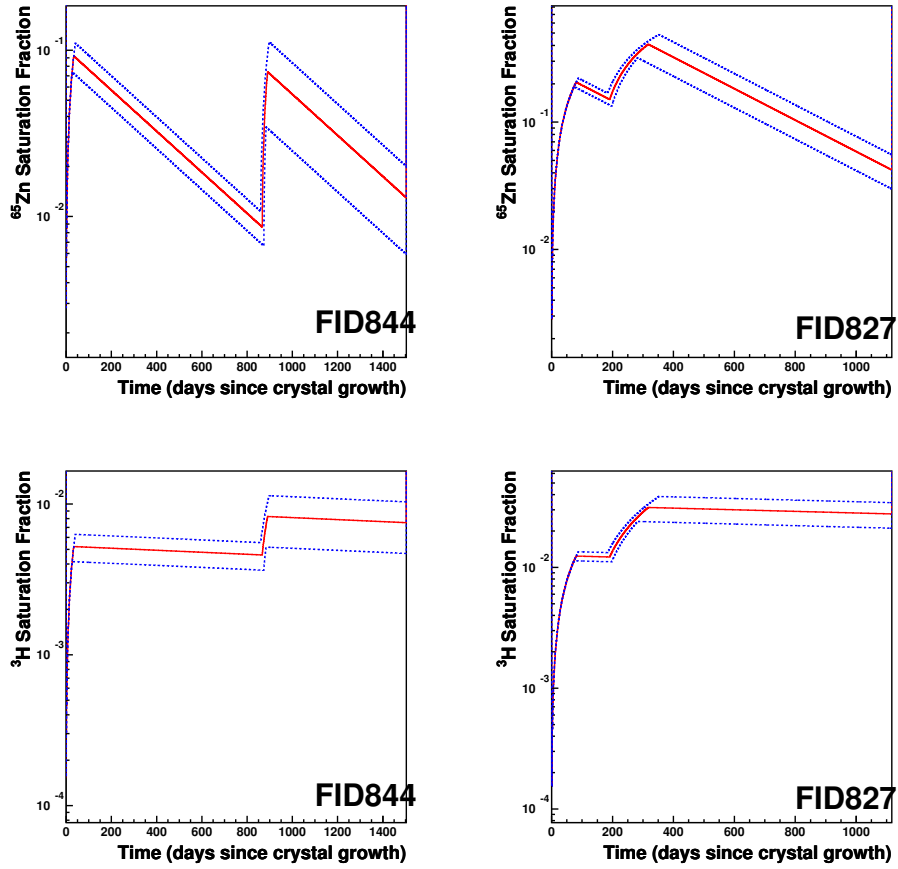
Figure 4: Saturation fraction f_s as a function of time for detector FID844 (standard history, left figure) and FID827 (longer t_{exp2}, right figure). Red plain lines represent the saturation fraction for the average t_{exp1}, t_{exp2}, t_{dec1} and t_{dec2}, whereas the blue bands represent the systematic uncertainty due to the history model considered. Top and bottom rows refer to ^{65}Zn and ^{3}H, respectively.
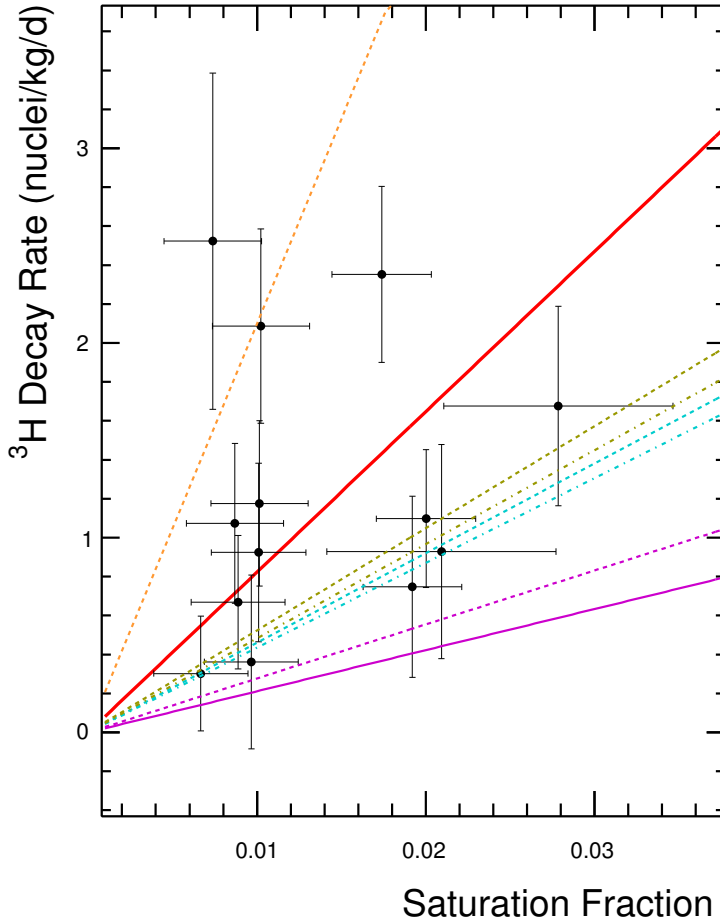
Figure 5: Tritium decay rate as a function of saturation fraction for thirteen detectors. Horizontal error bars show uncertainties in exposure and decay time periods. Vertical error bars include statistical and systematic errors. Red solid line represents the best fit. ACTIVIA [16] calculations performed within this work are shown as dashed and dashed-dotted light-blue lines using semi-empirical [19, 20, 21, 22, 23] and MENDL-2P [24] cross sections, respectively. Purple solid line represents an upper limit from IGEX data estimates in Ref. [5]. Previous calculations have been included as dashed lines: Mei et al. [5] using TALYS cross sections (purple), an update of this latter from Zhang et al. [17] using GEANT4 (olive-green dashed line) and ACTIVIA (olive-green dotted-dashed line) and Avignone et al. [4] from [28] (orange).
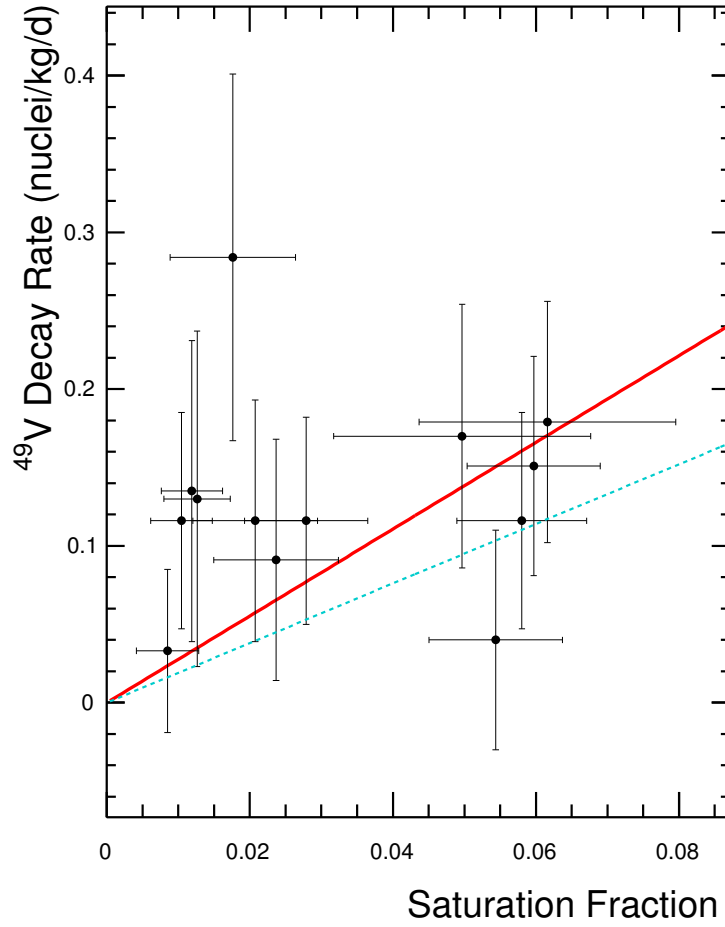
Figure 6: ^{49}V decay rate as a function of saturation fraction for thirteen detectors. Horizontal error bars show uncertainties in exposure and decay time periods. Vertical error bars include statistical and systematic errors. Red solid line represents the best fit. AC-TIVIA [16] calculations using semi-empirical [19, 20, 21, 22, 23] and MENDL-2P [24] cross sections performed within this work give the same result that is shown as dashed light-blue line.
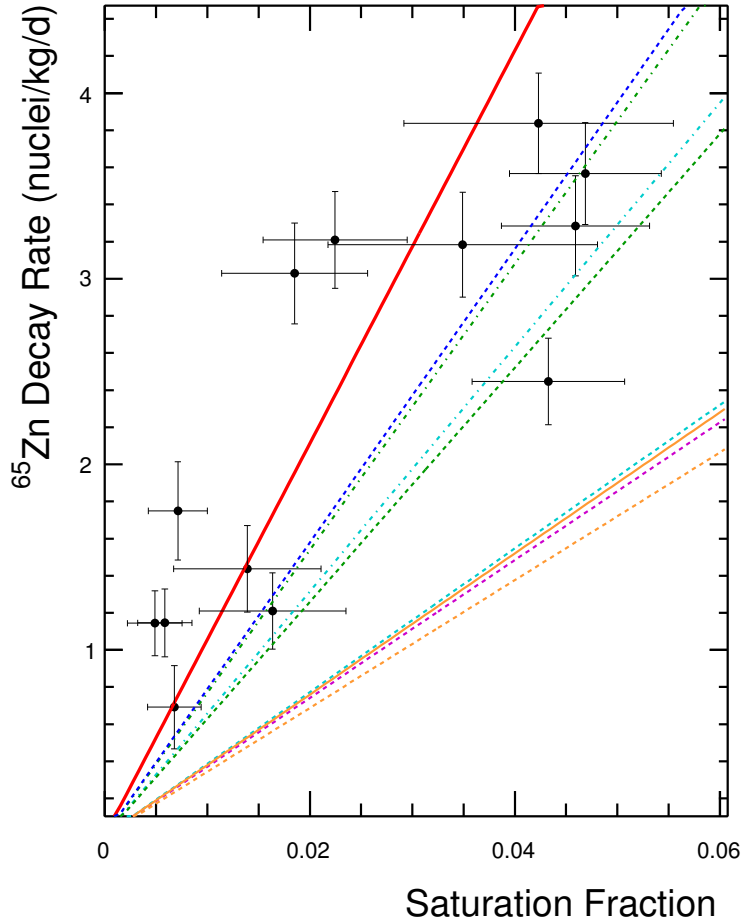
35

Figure 7: ^{65}Zn decay rate as a function of saturation fraction for thirteen detectors. Horizontal error bars show uncertainties in exposure and decay time periods. Vertical error bars include statistical and systematic errors. Red solid line represents the best fit. ACTIVIA [16] calculations performed within this work are shown as dashed and dashed-dotted light-blue lines using semi-empirical [19, 20, 21, 22, 23] and MENDL-2P [24] cross sections, respectively. Previous calculations have been included as dashed lines: Klapdor-Kleingrothaus et al. [27] (dark blue), Mei et al. [5] using TALYS cross sections (purple), Avignone et al. [4] (orange). The calculations from Ref. [26] that assume Ziegler [15] and Gordon et al. [18] cosmic neutron spectra are shown as green dotted and dashed-dotted lines, respectively. In addition, solid orange line shows previous experimental data from Ref. [4].
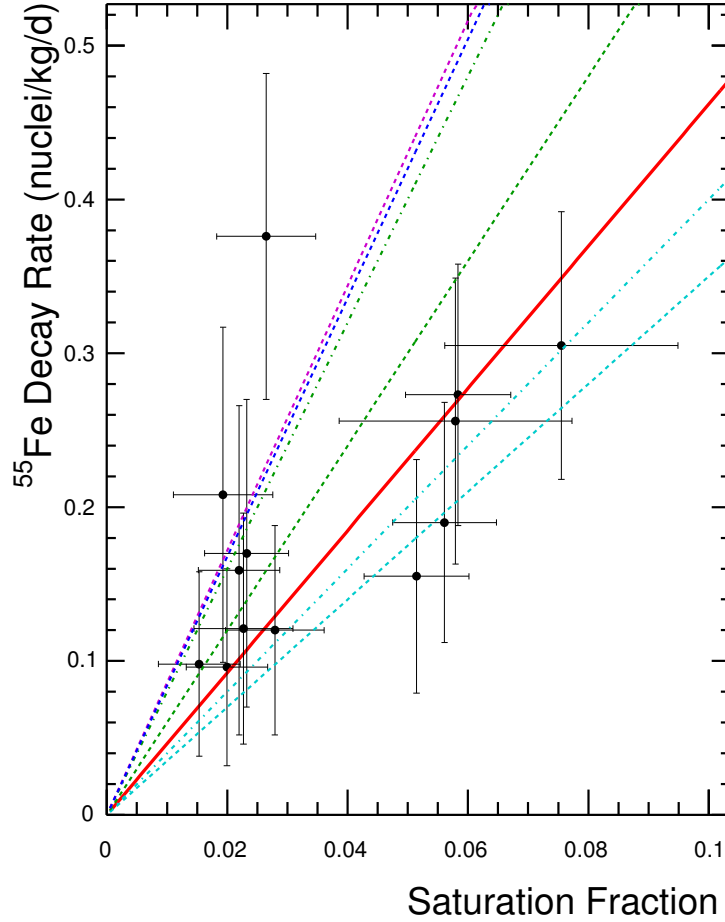
Figure 8: ^{55}Fe decay rate as a function of saturation fraction for thirteen detectors. Horizontal error bars show uncertainties in exposure and decay time periods. Vertical error bars include statistical and systematic errors. Red solid line represents the best fit. ACTIVIA [16] calculations performed within this work are shown as dashed and dashed-dotted light-blue lines using semi-empirical [19, 20, 21, 22, 23] and MENDL-2P [24] cross sections, respectively. Previous calculations have been included as dashed lines: Klapdor-Kleingrothaus et al. [27] (dark blue), Mei et al. [5] using TALYS cross sections (purple). The calculations from Ref. [26] that assume Ziegler [15] and Gordon et al. [18] cosmic neutron spectra are shown as green dotted and dashed-dotted lines, respectively.
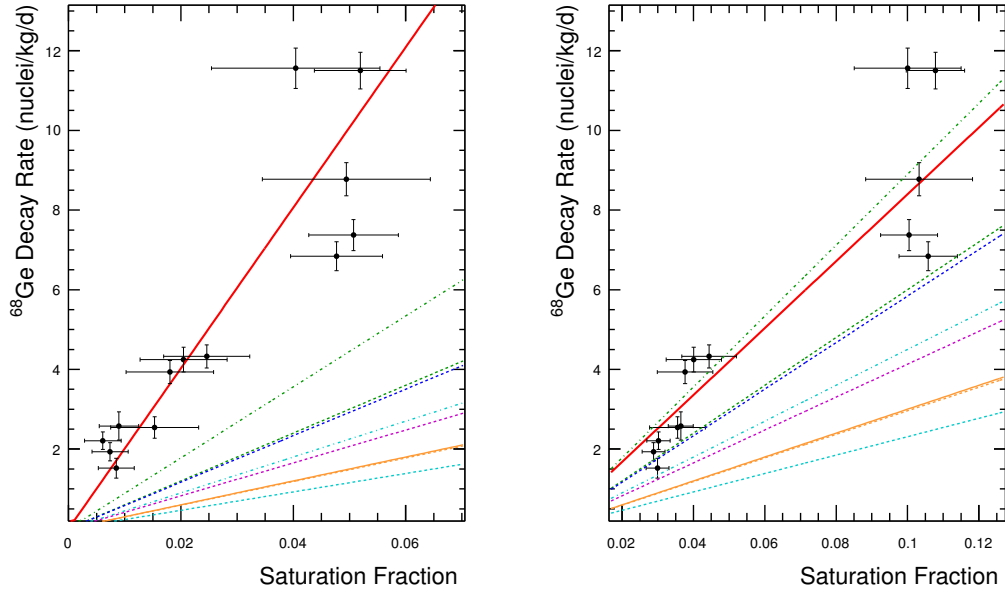
Figure 9: ^{68}Ge decay rate as a function of saturation fraction for thirteen detectors. Horizontal error bars show uncertainties in exposure and decay time periods. Vertical error bars include statistical and systematic errors. Red solid line represents the best fit. ACTIVIA [16] calculations performed within this work are shown as dashed and dashed-dotted light-blue lines using semi-empirical [19, 20, 21, 22, 23] and MENDL-2P [24] cross sections, respectively. Previous calculations have been included as dashed lines: Klapdor-Kleingrothaus et al. [27] (dark blue), Mei et al. [5] using TALYS cross sections (purple), Avignone et al. [4] (orange). The calculations from Ref. [26] that assume Ziegler [15] and Gordon et al. [18] cosmic neutron spectra are shown as green dotted and dashed-dotted lines, respectively. In addition, solid orange line reflects previous experimental data in Ref. [4]. Left panel represents the saturation fraction and production rate fit considering the standard detector history, whereas the right panel considers an additional 3-year exposure before the crystallization process. It reflects the saturation of ^{68}Ge.